

Received September 8, 2018, accepted October 23, 2018, date of publication November 5, 2018, date of current version December 3, 2018.

Digital Object Identifier 10.1109/ACCESS.2018.2879633

# Variable Stiffness Robotic Hand for Stable Grasp and Flexible Handling

SABER MAHBOUBI<sup>1</sup>, STEVEN DAVIS, AND SAMIA NEFTI-MEZIANI

School of Computing, Science and Engineering, University of Salford, Salford M5 4WT, U.K.

Corresponding author: Saber Mahboubi (saber.mahboubi@gmail.com)

This work was supported by the People Programme (Marie Curie Actions) of the European Union's Seventh Framework Programme FP7/2007-2013/ under REA Grant 608022.

**ABSTRACT** Robotic grasping is a challenging area in the field of robotics. When interacting with an object, the dynamic properties of the object will play an important role where a gripper (as a system), which has been shown to be stable as per appropriate stability criteria, can become unstable when coupled to an object. However, including a sufficiently compliant element within the actuation system of the robotic hand can increase the stability of the grasp in the presence of uncertainties. This paper deals with an innovative robotic variable stiffness hand design, VSH<sub>1</sub>, for industrial applications. The main objective of this paper is to realize an affordable, as well as durable, adaptable, and compliant gripper for industrial environments with a larger interval of stiffness variability than similar existing systems. The driving system for the proposed hand consists of two servo motors and one linear spring arranged in a relatively simple fashion. Having just a single spring in the actuation system helps us to achieve a very small hysteresis band and represents a means by which to rapidly control the stiffness. We prove, both mathematically and experimentally, that the proposed model is characterized by a broad range of stiffness. To control the grasp, a first-order sliding mode controller is designed and presented. The experimental results provided will show how, despite the relatively simple implementation of our first prototype, the hand performs extremely well in terms of both stiffness variability and force controllability.

**INDEX TERMS** Variable stiffness hand, stable grasp, force control, sliding mode control (SMC).

## I. INTRODUCTION

The uncertainty associated with miscalculated grasp models and/or objects with unknown mechanical parameters create difficulties in performing a stable grasp. Traditional approaches to eliminating this problem involve robotic hands that are expensive, delicate, complex and difficult to control. However, including a sufficiently compliant element within the actuation system of the robotic hand can provide an alternative solution to this challenge. Integrating such a passive component into a robotic system will increase the stability of the grasp in the presence of uncertainties. This is also true in the human hand, as it has been demonstrated that the passive nonlinear dynamics of the joints in the human hand play a vital role in providing a stable grasp [1]–[7].

The passive behavior of the human body, and more specifically the human hand, is the result of a combination of both parallel and series compliance. This form of behavior at the metacarpophalangeal joints is largely due to the elasticity of the capsular ligament of the joints and muscle-tendon

units [6], where the latter contributes to the stiffness of the joints by generating force when the muscle or tendon is under some form of tension [7].

Most of the existing research on robotic systems with variable stiffness/compliance take inspiration from the human body, mainly because of the aim of developing artificial limbs [8]–[15]. However, certain fundamental concepts and ideas that arise from this line of research can be exploited in order to create a new generation of industrial robots, and more specifically industrial grippers/hands, which feature controllable stiffness for demanding industrial applications requiring flexibility in grasping tasks. In-depth discussions about human hand grasping and human body impedance modulation can be found in [1]–[8], to mention but a few. Following these and other similar studies, a plethora of variable stiffness/compliance designs have been proposed for robotic systems over the last decade [9]–[18].

One of the earliest attempts to produce compliant actuators was accomplished by Pratt and Williamson [14].

They suggested an elastic element should be placed between the conventional rigid actuators and external loads. They also developed one of the earliest impedance control methods for their serial elastic actuator. They showed some of the benefits of using such actuators, which include shock resistance, smaller sensible inertia, more precise and robust force control, safer interaction with the environment and energy storage properties. This actuator was used as the actuation system in the arms of the MIT humanoid robot “COG” [15], [16].

A compact rotational series elastic actuator was introduced in [18] and [19], for use in multi-DOF small-scale humanoid robots. The design consisted of six identical linear mechanical springs and a conventional DC motor. There were three rigid spoke elements connecting the central bearing (output shaft) of the actuator to the springs. This connection was used to transfer the elasticity of the springs to the main shaft and hence provide compliance at the shaft.

The Compact Rotary Series Elastic Actuator (cRSEA) was suggested by Kong *et al.* [20] and Woo *et al.* [21] to be used in human assistive limbs. They used a combination of a torsion spring and a chain of worm and spur gears in this design to reduce size and achieve precise torque control. To control the output torque of the actuator (assistive torque) they used real-time feedback of the joint angle and environmental contact force. The gear-spring mechanism in their system isolated the motor from the environment and hence could potentially be used as a shock absorber.

Tonietti *et al.* [22] and Bicchi *et al.* [23] proposed a variable stiffness actuator designed for use in robotic systems as well as any mechanical devices which require some form of physical interaction with their surrounding environment. The actuator consisted of two DC motors. The shaft of each DC motor was connected to a pulley. A timing belt connected the two DC motors and their associated pulleys to the output shaft. Three compression springs were used so as to create tension on the belt in their rest positions. In order to control the position of the output shaft, both DC motors were rotated in the same direction (and at the same speed), whereas the (remove the) rotation of the motors in the opposite direction changed the apparent stiffness of the output shaft.

A new compliant joint actuated by an antagonistically-twisted round-belt actuator was proposed by Inoue *et al.* [24], to be used in robotic applications. The design comprised two DC motors, one pulley, and a link connected to this pulley. Two twisting elastic and flexible round-belts connected the pulley to the shaft of the DC motors in an antagonistic setup. The contraction generated by twisting the belts was used to create a moment, and consequently rotational motion on the pulley [24].

In order to achieve a compliant leg for bipedal robots, a mechanically adjustable compliance and controllable equilibrium position actuator (MACCEPA1) was suggested in [25]–[27]. The MACCEPA consisted of three links and one common revolute joint (knee joint), where the links pivoted around the knee joint. There was also a lever link connected

to the knee. A linear tension spring was attached to the lever link and a string connected this spring to the lower link. The angle between the upper link and lever link could be changed by an electrical motor connected to the lever link. When the angle between lever link and the lower link was not zero, any elongation of the spring would generate a resistive torque, trying to line up the lower link with the lever link. When this angle was zero (the equilibrium position) the spring would not apply any resistive torque to the lower link. To generate an elongation on the spring and consequently a resistive torque, they used an electro-motor. This electro-motor was used to pull on the cable connected to the spring, which resulted in the pre-tensioning of the latter. This pre-tension changed the resistive torque for a given angle, consequently changing the apparent stiffness of the system.

Another relatively similar approach to the variable stiffness actuator was introduced in [28] and [29]. The model consisted of a linear compression spring connected to a low-friction roller on one side and a linear actuation mechanism on the other. Similar to MACCEPA, the role of the linear actuation system in this model was to generate a pre-tension on the linear spring by compressing it. The output link of the system was connected to a concave nonlinear cam and a revolute joint was used to connect this can to the main chassis. The roller was able to move inside the concave surface of the cam with a very low friction, with the associated motion used to generate the apparent stiffness of the output link. To change the apparent stiffness of the system, the linear motor was used to change the length of the spring and, consequently, the stiffness of the joint. The apparent stiffness of the system was a nonlinear function of the stiffness constant of the spring, the cam transmission ratio, and the offset of the output link. As mentioned, the design used a single actuator to change the output stiffness; however, the system was unable to control the output position (position of the output link).

A simplified model of the pulley-belt driven variable stiffness actuator was suggested by Grebenstein *et al.* [30], [31], and has been used as the actuation system in the DLR hand [32]. The model consisted of a DC motor, a pulley-tendon system and a slider-spring mechanism. The slider-spring mechanism was made of a linear compression spring, which was used to push the tendon in its rest position, forming the tendon into a triangle. To achieve an independent position and stiffness controllability in each joint, they used a pair of the mechanism detailed, in an antagonistic manner for each joint.

As explained before, the inherent passive properties of the human hand, in both serial and parallel combinations, play an important role in grasp stabilization [33]–[37]. Various studies into the grasp of the human hand have shown that as a preliminary response, to achieve a robust grasp, humans tighten their fingers by co-contracting antagonistic muscles and consequently increase the stiffness of the fingers just before perceiving impact [33].

Kajikawa and Abe [38] designed a four finger, twelve joint variable stiffness robotic hand for human care

service tasks. To reduce the number of the actuators in the hand, they suggested a linkage mechanism which coupled the distal and proximal interphalangeal joints and actuated these two joints via a single motor. To achieve compliance in the joints, they used silicon made from deformable cushions called SRC<sub>trans</sub>. An expandable cushion, SRC<sub>stiff</sub>, has been used to compress the SRC<sub>trans</sub> and consequently change the stiffness of the fingers. They used air pressure to inflate the SRC<sub>stiff</sub>.

A three-joint variable stiffness robotic finger was introduced by Yang and Chen [39]. Their design consisted of a soft pneumatic muscle and three pin heaters which were embedded in a shape memory polymer (SMP). The finger could bend by selectively heating the SMPs and due to internal air pressure of the pneumatic muscle. Additionally, the finger exhibited variable stiffness at different SMP's temperatures.

Yap *et al.* introduced a soft wearable exoskeleton glove for assistive and rehabilitation applications. They used embedded pneumatic actuators to actuate the exoskeleton. They showed that the stiffness of the fingers could be changed in different locations; however, this stiffness was not controllable [40].

Inspired by the human hand's tendon routings, and with the aim of improving the grasp stability and dexterity in manipulation tasks, a parallel compliant joint has been suggested for robotic fingers in [42]. The design consisted of a rectangular-shaped compliant material which was fixed between a pair of pulleys. The pulleys were fixed to the rotating shaft of the joints in such a way as to allow them to rotate with the fingers about the fingers' revolute joints. In order to fix the compliant part, they used two fixed pairs of pins. To prevent the compliant part from undergoing any undesired displacement, they used two clamps at the top of the pins. The rotation of the joint induced a tension on the compliant material, and consequently the compliant material created a passive torque due to its intrinsic properties.

To achieve appropriate mechanical impedance properties for the wide range of joint angles inherent to the human hand, they suggested a design optimization method. They used this method to optimize the design variables (radius of joints, pulley and pins, the distance between center of pulleys and joint and the thickness of the compliant component). Using an open-loop motion control to execute certain grasps, they experimentally proved that adding a parallel compliant component to the finger joints could improve the quality of the grasp. To emphasize the role of the suggested parallel stiffness, they first demonstrated that the feedback delay can destabilize the grasping task. Afterwards they concluded mathematically, as well as experimentally, that adding parallel compliance part to the gripper's joint can reduce the sensitivity of the gripper to this delay and consequently increase the stability of the grasp [36], [37].

Using polymer-based Shape Deposition Manufacturing (SDM), Odhner *et al.* [41] and Dollar *et al.* [43]–[45]

designed and fabricated an under-actuated, adaptive and compliant grasper. To increase the friction and prevent undesired slippage, the grasp side of each link contained a soft finger pad. A compliant joint flexure with a stiffness range between 0.0421 and 0.224 Nm/rad was used in the proximal and distal joints to connect the finger links. An embedded Hall Effect sensor in each joint was used to provide feedback regarding joint angle. A pre-stretched, nylon-coated, stainless-steel cable anchored into the distal link was used to transfer the actuation force from the actuator to the fingers and hence provide the motion. In zero actuation mode, the tendons, which were parallel with the flexible joints, remained slack, and hence the fingers remained in their maximum compliant mode. In actuation mode, however, the inelastic tendons reduced the flexibility of the fingers (increasing the fingers' stiffness), consequently increasing the accuracy of the grasp. The stiffness constant of the joints was 0.19 Nm.deg for both proximal and distal joints, as based on the optimization studies they developed to create a functional grasper. They showed that this stiffness enables the grasping of the widest range of object sizes with the greatest amount of uncertainty in object position [45]. They also showed that the uncertainty of the grasping tasks can be satisfactorily accommodated by having optimal compliance and adaptability in the mechanical design of the hand. The experimental results provided demonstrated the robustness of the SDM hand in grasping objects in the presence of large positional errors [50].

Pettersson *et al.* proposed a gripper mechanism that utilized the magnetorheological (MR) fluid in its variable impedance actuation mechanism. The gripper was designed for pick and place tasks in natural food product companies where the objects have different shapes and can be easily squashed. Reducing the risk of bruising through variable impedance gripping was the main advantage of the design, as claimed in [46].

Maekawa *et al.* developed a three-fingered robot hand with a new method of controlling stiffness. Briefly, the hand was formed from three fingers, each of which included three joints. A tendon-sheath actuated by D.C. servo motor was the driver mechanism for each joint. An embedded potentiometer and a new tension differential-type torque sensor were used to provide torque feedback from each joint. They proposed a stiffness control scheme to control the apparent stiffness of the hand. By using the joints' positions and torque feedback, the controller was controlling both the position and stiffness of the joints and, consequently, controlling the grasp impedance. Finally, they validated the proposed mechanism and designed a position-stiffness control method by conducting various grasping experiments [47].

Inspired by human hand, Lau and Chai designed a low cost, variable stiffness anthropomorphic robotic hand using pneumatic artificial muscles. Their proposed anthropomorphic design consisted of 16 DOFs in which 14 pneumatic air muscles were used to actuate the tendon-driven fingers.

They used an open-loop control scheme to control the fingers' positions and stiffnesses. The hand was able to perform some basic grasps [48].

RAMA-1 was a highly dexterous 48 DOF robotic hand designed by Rasakatla and Krishna [49]. The robot consisted of joints which were based on magnetic sliding and spherical spheres and used tendons to actuate the fingers. It provided more degrees of freedom than the human hand. The new six DOF thumb in this hand had a greater range of motion than the ordinary thumb and improved the overall dexterity and manipulability of the hand. They tried to simplify the process and control task for robust grasping. They demonstrated through experiment that using an optimized passive compliant joint and adaptive coupling in the hand increases the adaptability of the large positioning errors that can occur in unstructured grasping tasks.

To control the mechanical impedance of the fingers in a flexible joint hand, two new control designs were proposed in [51]. The target impedance in the authors' grasp model was based on the desired stiffness and damping, though they neglected the inertia term of the impedance in their model. The two suggested cascade controllers consisted of one inner torque-feedback loop, and an outer impedance control loop. They used a physical interpretation of the rotor inertia to estimate the torque in the inner loop of the controllers. They then designed two different outer impedance controllers. The first controller used a combination of the motor shaft's position and the system's stiffness and damping term to control the impedance of the grasp, whereas in the second controller these parameters were merged such that under steady-state conditions the desired equilibrium position could be satisfied. They also demonstrated that both controllers could be adapted to the visco-elastic properties of the joints. They experimentally verified the concept of the controllers using a DLR lightweight hand.

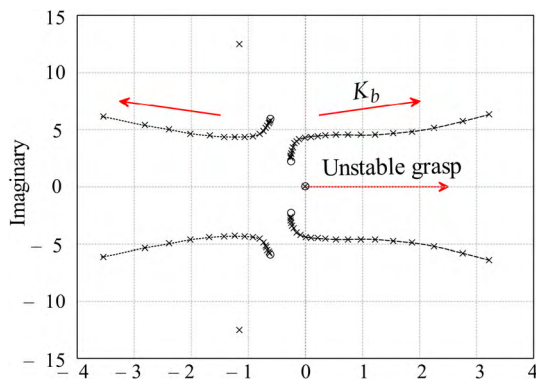


**FIGURE 1.** Root locus plot for the gripper-object model. The mechanical properties of the object (stiffness,  $K_b$ ) can move the system's poles to the right side of the root locus plot, which leads to unstable grasp.

To conclude, any uncertainty inherent to the grasp model can easily destabilize the interaction port (fingers-object contact point) of the grasp when controlled by a conventional fixed gain control method. Fig. 1 illustrates how the

mechanical properties of the object (stiffness,  $K_b$ ) can move the system's poles to the right side of the root locus plot, which leads to the grasp being destabilized.

One of the traditional approaches to eliminating this undesired destabilizing effect is to include a passive elastic element between the fingers and actuator. This passive element can increase the stability of the system in the presence of such uncertainties. A range of variable stiffness/compliance designs have been reviewed and discussed in this section.

Although the variable stiffness mechanisms reviewed can still, to some extent, increase the stability of the system when interacting with the environment, their application in real-world industrial scenarios is still somewhat lacking. As far as grippers/hands are concerned, the complexity of the design, small operational force and stiffness range, weight, durability and cost issues are amongst the various reasons that might cause industry to insist on the continued use of traditional stiff mechanisms.

This paper deals with an innovative robotic variable stiffness hand design, VSH<sub>1</sub>, for industrial applications. The proposed passive, adjustable compliance, serial elastic actuation system introduced in this paper is suitable for industrial applications which greatly reduces the limitation of the maximum achievable stiffness. Our design consists of only two servo motors, the combined motion of which are used to drive the fingers and change the compliance of the joints. Non-stretchable tendon is used to transfer the actuating force to the fingers. The design provides a fast response solution by which to control the grip impedance; simplicity of design, small hysteresis band and affordability, as well as durability, are amongst their advantages. The overall architecture of the concept is based on the principle that a simple mechanism provides inherent robustness and reliability and, therefore, is able to withstand the severe working conditions inherent to the long and repetitive tasks typical of production lines.

The remainder of this paper is organized as follows: Section II. A provides an overview of our proposed variable stiffness hand, called VSH<sub>1</sub>, followed in sub-section B, by a discussion of the stiffness model in both stiff and compliant status and the mathematical modeling of the hand's apparent stiffness and its associated force-displacement function. In Section III a report on the experimental results on the hand's performance for different stiffness values will be given.

Sections IV provides a discussion on the first-order sliding mode control method we designed and validated (in Section V) to control the grip force. The paper will end with final discussion and conclusions in Section VI. Note that the terms "stiffness" and "compliance" and related adjectives ("compliant," "stiff") are used herein to indistinctly characterize, as opposing terms, the non-rigid behavior of the gripper actuation system.

## II. VARIABLE STIFFNESS HAND (VSH1)

In this section we introduce the design of a novel variable stiffness hand (VSH<sub>1</sub>) for industrial robotic manipulators,

which can be used for stable grasps (as discussed before) with unknown objects to be grasped, as well as to control the applied grip force in the absence of any accurate force sensor.

**A. DESIGN EXPLANATION**

Similar to the majority of variable stiffness mechanisms that are referenced in this paper, our design consists of two rotational electric actuators. The actuators are two identical 7 Nm servo motors whose mechanical and electrical details are reported in Table 1. A side view of VSH<sub>1</sub> with two different versions of fingers (two finger, two joints (left) and three finger, six joints (right) can be seen in Fig. 2. As shown in this figure, both versions of the VSH<sub>1</sub> use an identical actuation system to actuate the fingers.

**TABLE 1. Mechanical and electrical specification of the servos used in VSH<sub>1</sub>.**

Dynamixel motor Model MX-64T			
Torque	5.5N.m (11.1V,3.9A)	6N.m (12V,4.1A)	7.3N.m (14.8V,5.2A)
Speed	58rpm (11.1V)	63rpm (12V)	78rpm (14.8V)
Communication Protocol	TTL		
Baud rate	8000 bps ~ 4.5Mbps		
Controller	PID		
Resolution	0.088 Degree		
Weight	126 g	Dimension	40.2 × 61.1 × 41 mm

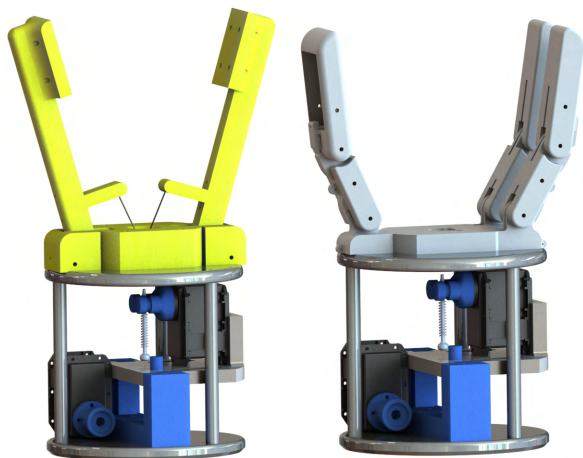
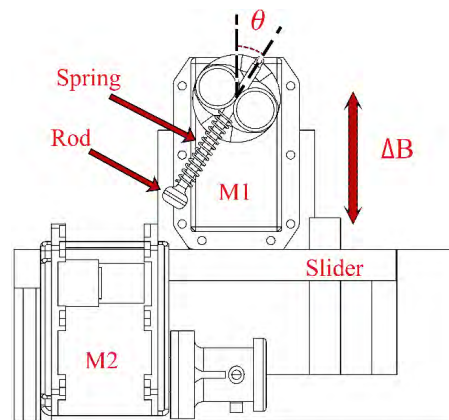
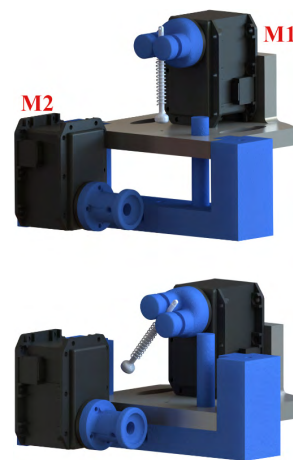


**FIGURE 2. The VSH<sub>1</sub> introduced in this paper with two different versions of fingers (two finger, two joints (left) and three finger, six joints (right)).**

The two servo motors also can be seen in this figure. One of the servos, M<sub>1</sub>, provides rotational motion  $\theta$ , whilst the second is used to produce a linear displacement,  $\Delta B$ , along the wrist axis of the gripper. Fig. 3 depicts these servos and their corresponding motions. As can be seen from this figure, a tendon-pulley-slider arrangement is used to transform the rotational motion of M<sub>2</sub> to achieve linear displacement. We used this linear motion to move the slider along the wrist



(a)



(b)

**FIGURE 3. (a) A CAD model and (b) a schematic representation of our VSH<sub>1</sub>. Our design consists of two rotational electric actuators M<sub>1</sub> and M<sub>2</sub>. One of the servos, M<sub>1</sub>, provides rotational motion  $\theta$ , whilst the second is used to produce a linear displacement,  $\Delta B$ , along the wrist axis of the gripper.**

axis of VSH<sub>1</sub> as shown in this figure. Motor M<sub>1</sub> is mounted on this slider and follows the slider’s movements. As shown in the figure, there is a linear compression spring connected to the shaft of M<sub>1</sub> through a rigid rod. Fig. 3 also depicts a pair of pins in the center of the shaft. We use these pins to hold the rod and spring. The rod slides through the pins and across the shaft’s axis. The linear compression spring is placed around the rod, also as shown.

A spring holder pin in the bottom of the rod holds the spring in place. To transfer the driving force from the actuator to the fingers, a tendon establishes the connection between the rod and fingers.

The subsequent tendon-rod-spring configuration generates a compliance behavior for the hand which will be explained in the upcoming sections. Any external force on the hand’s fingers will generate a tensile force which will be transferred to the rod-spring system via the tendon. The force transferred to the rod will pull it, and consequently compress the spring where, as will be explained in the following section, the magnitude of this compression is a function of the force and  $\theta$ .

**B. WORKING PRINCIPLE AND MODELING**

In this section, we will explain the working principle of our variable stiffness mechanism. To do so, as depicted in Fig. 4, we use two coordinate frames: (a) the reference coordinate frame OXYZ, and (b) the shaft coordinate frame  $o'x'y'z'$  which is parallel to the reference coordinate frame. We assume that the shaft coordinate frame is fixed to the shaft of  $M_1$  in such a way that  $o'$  is in this shaft's geometric center, as shown in the Figure. From this figure, the rotational motion of  $M_1$  is around  $x'$  axis of  $o'x'y'z'$  and the linear motion of  $M_2$  is along the Y direction of OXYZ. The combination of motions of  $M_1$  and  $M_2$  provides the ability to independently control the stiffness and position of the fingers, as will be explained below.

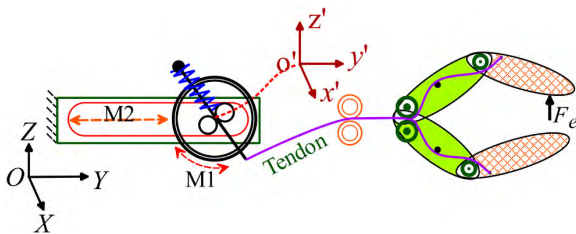


**FIGURE 4.** Schematic model of the proposed three finger VSH<sub>1</sub>. The integrated tendon transfers any external force from the fingers to the rod-spring mechanism. The combination of the motions of M<sub>1</sub> and M<sub>2</sub> provides the ability to change the stiffness and position of the fingers.

In Fig. 4, the purple line represents the tendon that establishes the connection between the rod and fingers. As already mentioned, this tendon is used to transfer the driving force from the variable stiffness mechanism to the fingers. The apparent stiffness of the fingers,  $\delta_o$ , is dependent on the angle between the rod and tendon, and this stiffness changes according to this angle. We use  $M_1$  to change this angle, and hence control the stiffness of the fingers.

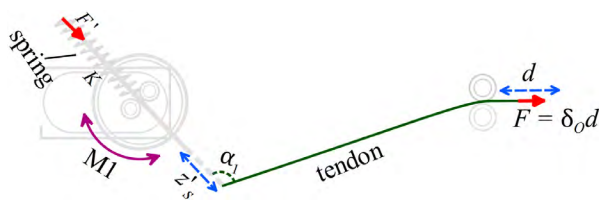


**FIGURE 5.** The tendon is pulled by  $F$  and the spring is compressed due to this force. The output stiffness of the hand,  $\delta_o$ , is a function of  $\alpha_1$ .

Now let us remove the hand from its actuation system and assume that the tendon is pulled by an external force,  $F$ , as shown in Fig. 5. Hence, we can write:

$$|F \cos \alpha_1| = KZ'_s \tag{1}$$

Where  $\alpha_1$ , as shown in the figure, is the angle between the rod and tendon,  $Z'_s$  is the amount of compression in the spring due to the force  $F$ , and  $K$  denotes the spring constant. From (1) we can write:

$$Z'_s = \frac{|F \cos \alpha_1|}{K} \tag{2}$$

We assume that the rotation of the servo motor  $M_1$  is bounded as below:

$$0 \leq \theta \leq \frac{\pi}{2} \tag{3}$$

From Fig. 5, (3) and (2) we can write:

$$\begin{aligned} \pi &\leq \alpha_1 \leq \frac{\pi}{2} \\ 0 &\leq |Z'_s| \leq \frac{|F|}{K} \end{aligned} \tag{4}$$

Equation (4) illustrates the minimum and maximum compression of the spring (which is equal to the displacement of the rod) due to the external force  $F$  on the tendon. In this equation, zero compression corresponds to  $|\alpha_1| = \pi/2$ ; assuming the motors are non-back drivable, the tendon is inelastic, and the shear deformation of the rod is negligible, we can thus write:

$$|\alpha_1| \rightarrow \frac{\pi}{2} \quad \delta_o \rightarrow \infty \tag{5}$$

and

$$\min \delta_o = K |_{\alpha_1=\pi} \tag{6}$$

where  $\delta_o$  is the output stiffness of the variable stiffness mechanism. Fig. 6 shows the hand in both its open and closed states with minimum and maximum stiffness. In this figure, the red hands correspond to the stiff fingers with the maximum (ideally infinite) stiffness, whilst the blue ones correspond to the fingers with minimum stiffness, which is equal to the stiffness of the spring,  $K$ .

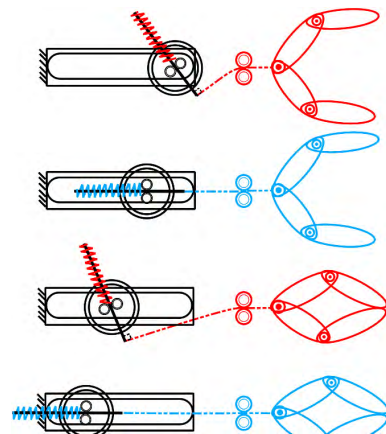


**FIGURE 6.** VSH<sub>1</sub> in its maximum (red) and minimum (blue) stiffness configurations. In both states related to the hand with maximum stiffness, the angles between the tendon and rod are a right angle and for the blue hands, which correspond to the minimum stiffness, the tendon lies along the rod and spring.

As shown in this figure and from (5) and (6), in both states related to the hand with maximum stiffness, the angles between the tendon and rod are perpendicular, and for the blue hands, which correspond to the minimum stiffness, the tendon lies along the rod and spring ( $\alpha_1 = \pi$ ).

In order to derive the stiffness function of the hand, let us assume that the displacement of the tendon due to the above-mentioned external force is equal to  $d$ . Fig. 7 depicts this

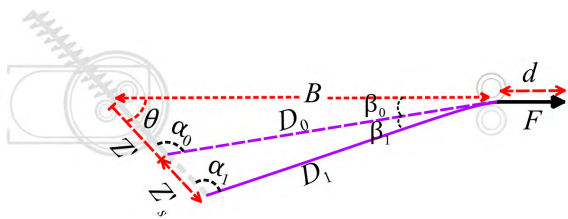


**FIGURE 7.** Position of the rod and tendon before and after application of force  $F$ . The solid purple line corresponds to the tendon before applying force, whilst the dashed purple line corresponds to the tendon after application of force.

force and its associated displacement. For clarity, we have not shown the hand in this figure.  $D_0$  represents the distance between rod's end point (tendon-rod fixing point) and the wrist of the hand.  $Z'$  is the length between rod's end point and the center of the shaft of  $M_1$  before applying the force.  $D_1$  is the distance between rod's end point and the wrist after applying the force.  $Z'_s$  shows the displacement of the rod's end point due to compression of the spring after applying the force. Using the law of sines, we can write

$$\sin \theta = \frac{D_0 \sin \alpha_0}{B} \quad (7)$$

where  $\theta$  is the angle between the rod and Y-axis,  $B$  is the distance between the center of the shaft of  $M_1$  and wrist point of the hand, and  $\alpha_0$  is the angle between the tendon and rod in their initial positions. After applying the force, and by using (7), we can write:

$$\frac{\sin \alpha_1}{B} = \frac{D_0 \sin \alpha_0}{BD_1} \quad (8)$$

Assuming that the tendon is perfectly inelastic, we can write:

$$D_1 = D_0 - d \quad (9)$$

Using (8) and (9) we have:

$$\alpha_1 = \sin^{-1} \frac{D_0 \sin \alpha_0}{(D_0 - d)} \quad (10)$$

And by again using the sine law and (9), we can get:

$$\frac{\sin(\beta_0 + \beta_1)}{z' + z'_s} = \frac{\sin \theta}{D_0 - d} \quad (11)$$

where  $\beta_0$  and  $\beta_1$  are shown in Fig. 7. By simple calculation, we get:

$$\beta_1 = \alpha_0 - \alpha_1 \quad (12)$$

substituting (12) into (11) we obtain:

$$z'_s = \frac{(D_0 - d) \sin(\beta_0 + \alpha_0 - \alpha_1)}{\sin \theta} - z' \quad (13)$$

Finally, from (10) and (13) we can conclude:

$$z'_s = \frac{(D_0 - d) \sin\left(\beta_0 + \alpha_0 - \sin^{-1}\left(\frac{D_0 \sin \alpha_0}{(D_0 - d)}\right)\right)}{\sin \theta} - z' \quad (14)$$

Also, from Fig. 6 we have:

$$F' = -F \cos \alpha_1 = Kz'_s \quad (15)$$

where  $F'$  is the decomposed element of  $F$  along the rod axis. Adding (10) and (14) to (15) we can write:

$$F = \frac{K(d - D_0) \sin\left(\beta_0 + \alpha_0 - \sin^{-1}\left(\frac{D_0 \sin \alpha_0}{(D_0 - d)}\right)\right) + z' \sin \theta}{\cos\left(\sin^{-1}\left(\frac{D_0 \sin \alpha_0}{(D_0 - d)}\right)\right) \sin \theta} \quad (16)$$

where:

$$\begin{cases} D_0 = \sqrt{B^2 + z'^2 - 2Bz' \cos \theta} \\ \beta_0 = \sin^{-1}\left(z' \left(\frac{\sin \theta}{D_0}\right)\right) \end{cases} \quad (17)$$

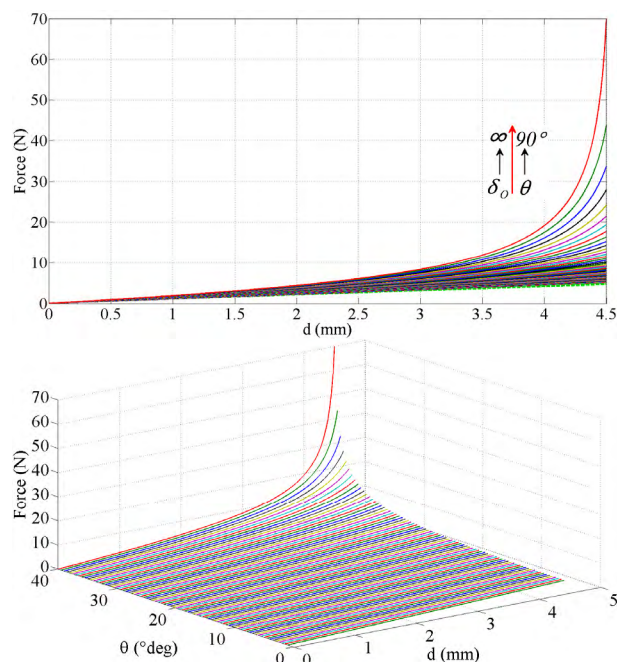


**FIGURE 8.** Stiffness of the hand (fingers),  $\delta_o$ , for different values of  $\theta$ . This stiffness increases with increasing  $\theta$ . The set of curves demonstrates how  $d$  changes when  $F$  varies over a discrete range of  $\theta$  (from 0 to 40°) in two different views.

Equation (16) and (17) formalize the relationship between the applied force  $F$  and  $d$  for different  $\theta$ , which entails the nonlinearity of the output stiffness  $\delta_o$ . The set of curves in Fig. 8 shows how  $d$  changes when  $F$  varies over a discrete range of  $\theta$  (from 0 to 40°) in two different views. In these figures, the lowest line shows the stiffness of the fingers when  $\theta = 0$  ( $\alpha_1 = \pi$ ). As expected, due to the linear spring used in our actuator, there is a plateau in the force-displacement relationship for this angle. The slope of this line is equal to the stiffness of the integrated spring,  $K$ . From this figure, and entirely as expected, the slopes of the curves increase with increasing  $\theta$  as the highest line, the red curve, is associated to the greatest angle  $\theta = 40^\circ$ .

In more generic terms, the stiffness of a grasp can be modeled by a relationship between the applied force and the

displacement due to this force [52]:

$$\delta_O^\theta = \left. \frac{\partial F}{\partial d} \right|_\theta \quad (18)$$

where the term  $\delta_O^\theta$  highlights the dependence of the grasp's stiffness on the angle  $\theta$ . As shown in Fig. 8, this stiffness increases with increasing  $\theta$ . It is worth noting that from (16) and (17), the fingers' stiffness,  $\delta_o$ , is also dependent on the stiffness of the spring  $K$  and the variable  $B$ . Fig. 9 shows the effect of different values of  $K$  and  $B$  on the output stiffness of the hand. As can be noted from this figure, the output stiffness of the hand (fingers' stiffness) increases with increasing  $K$  and/or  $B$ .

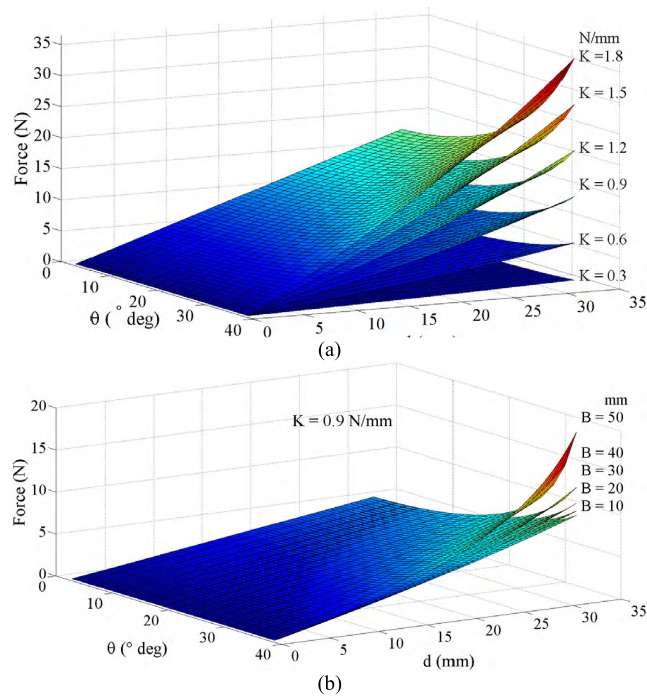


FIGURE 9. Stiffness of the hand,  $\delta_o$ , for different values of  $K$  and  $B$ . The output stiffness of the hand (fingers' stiffness) increases with increasing (a)  $K$  and (b)  $B$ .

### III. EXPERIMENTAL RESULTS AND VALIDATION

To validate the concept of the variable stiffness hand, we fabricated our tendon-driven hand prototype, VSH<sub>1</sub>, (Fig. 10), as characterized by three fingers and six joints (two joints per finger). This figure shows the hand and its ability to grasp objects of different stiffnesses, shapes and weights. In Fig. 11, we report actual measurements of the displacement  $d$  for different values of applied force in the presence of different rotations of  $M_1$  ( $\theta = 5^\circ, 10^\circ, 15^\circ, 20^\circ, 25^\circ, 30^\circ, 40^\circ$  and  $55^\circ$ ). To collect these data, we used a spring with a stiffness constant of 0.3 N/mm in VSM<sub>1</sub>. To collect the experimental results, we removed the hand from the actuation system and, by hanging different weights on the tendon, we measured the associated elongation of the tendon,  $d$ .



FIGURE 10. VSH<sub>1</sub> with three finger can grasp different objects with different sizes and flexibilities thanks to its variable stiffness mechanism.

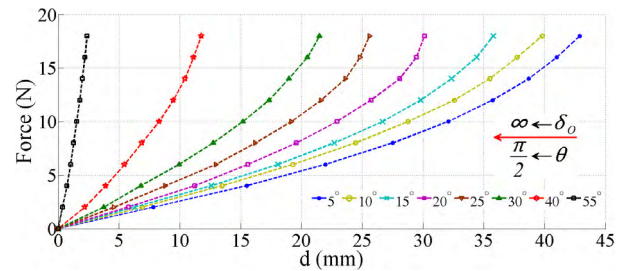


FIGURE 11. Experimental measurements of the displacement  $d$  for different values of applied force and rod angles ( $\theta = 5^\circ, 10^\circ, 15^\circ, 20^\circ, 25^\circ, 30^\circ, 40^\circ, 55^\circ$ ). The output stiffness of the hand increases with increasing  $\theta$ .

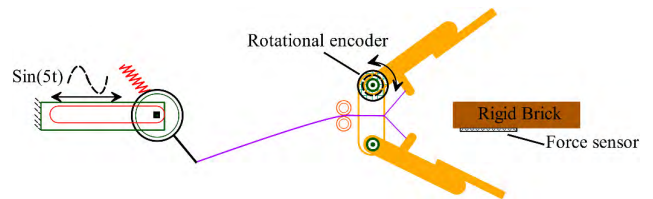


FIGURE 12. Hardware setup for the trajectory tracking experiment. This experiment shows the capability of the fingers to follow a desired trajectory in the presence of different stiffnesses. To stop the fingers in their movement at a certain position, a rigid brick placed between the fingers. A rotational encoder and a FSR sensor was used to measure the rotation of the fingers about the fingers' joint and the grip force.

To test the capability of the fingers to follow a desired trajectory in the presence of different stiffnesses, a trajectory tracking experiment was performed using a  $\text{Sin}(5t)$  motion input applied to  $M_2$ . Fig. 12 depicts a schematic model of the hardware setup of this experiment. The output of this experiment was the rotation of the fingers (left finger in the figure) about the fingers' joint. This rotation has been measured by a rotational encoder mounted on the joint of the left finger. Fig. 12, also depicts a fire brick placed between the fingers. This brick was used to stop the fingers in their movement at a certain position. A FSR (Force Sensitive Resistor) sensor was mounted on this brick to measure the grip force. The main technical specifications of the sensor are reported in Table 2. Fig. 13 shows the experimental results collected from this experiment. To perform this test, we set the angle  $\theta$  to  $0^\circ, 10^\circ, 20^\circ$  and  $30^\circ$  where the subplots a, b, c and d show the finger trajectories associated to these angles, respectively.



**TABLE 2.** Specification of the force sensor used in our hand.

Force sensitivity range	< 20 g to > 10 kg
Pressure sensitivity range	< 1.5 psi to > 150 psi
Force resolution	5 g
Sensitivity to noise/vibration	Not significantly affected

The green dashed lines in this figure depict the desired input trajectory (applied to  $M_2$ ), whereas the solid blue lines show the actual motion of the fingers measured by the encoder. As shown in this figure, the increased stiffness of the fingers acts to stabilize the system where the finger with higher stiffness ( $\theta = 30^\circ$ ) follows the sinusoidal trajectory with a reduced error.

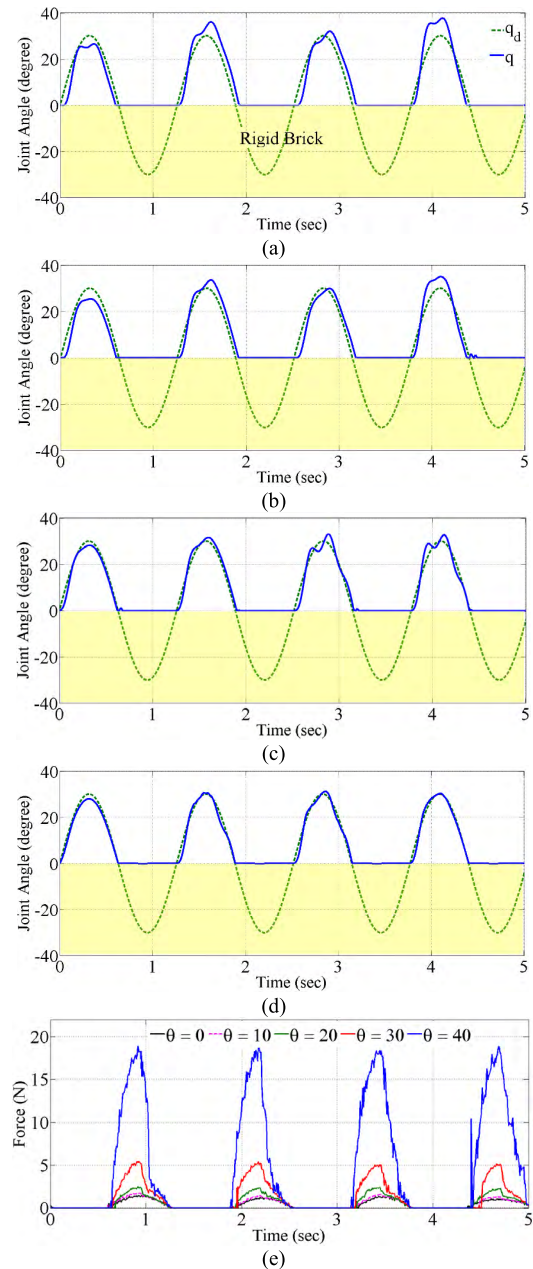
Fig. 13.e depicts the grip force applied by the hand to the fire brick, as measured through the FSR sensor. The figure shows that the applied force increases by increasing the value of  $\theta$  and, consequently, the stiffness. The smallest force (the black dashed line in the figure) measured for the test was for the smallest  $\theta$ , which corresponds to the smallest stiffness. As this figure shows, the grip force was increased with increasing  $\theta$ . This was expected, as larger  $\theta$  corresponds to the greater stiffness of the finger, so for a given displacement, the larger stiffness must generate the greater force.

Fig. 14 shows the stiffness hysteresis curves for different values of the rod angle,  $\theta$ , obtained by gradually applying an external force and measuring the associated displacement,  $d$  and then gradually removing this force. To perform this experiment, we used a spring with a spring constant of 0.55 N/mm. Clearly this hysteresis could be narrowed through a better design aimed at reducing friction and damping in the mechanical couplings.

Finally Fig. 15 depicts the magnitude bode plot of the fingers' motion for different values of  $\theta$ . As expected, it can be seen that the peak magnitude decreases with increasing  $\theta$ , consequently increasing the stiffness of the finger.

#### IV. FORCE CONTROL FOR THE VSH<sub>1</sub>

In this section we discuss the sliding mode force control architecture we designed to control the grip force in our variable stiffness hand. A schematic model of the hand is illustrated in Figure 16. For clarity, the mechanical connections for only one finger and the actuation system are shown in this figure. The two masses,  $M_F$  and  $M_R$ , describe the mass of the finger and rotor mass of the second servo motor,  $M_2$ , respectively. The spring  $K_v$  in this figure is used to model the output nonlinear (variable) stiffness term where  $K_v = \delta o$ .  $K_b$  is used to model the stiffness of the grasped object. The dampers,  $B$  and  $B_R$ , are used to model the friction between the fingers and palm, and the friction between the rotor and stator of the DC motor (the friction of the shaft bearings and friction between the commutator and brushes of  $M_2$ ), respectively. For simplicity, the friction between the rod and pins is neglected. Finally, the stiffness and damping terms,  $K_J$  and  $B_J$ , are used to model the stiffness and frictional losses



**FIGURE 13.** (a, b, c, d) Finger's motion (solid lines) versus desired trajectory (dashed lines) for the sinusoidal trajectory tracking experiment for  $\theta = 0^\circ, 10^\circ, 20^\circ$  and  $30^\circ$  respectively. (e) FSR sensor measurements of the grip force exerted by the fingers on the brick.

of the sliding system, respectively. As shown in the figure, the rotor is driven by the motor magnetic field force,  $F_a$ .

Equation (19) depicts a second-order system that we use to model our hand and its DC servo motor,  $M_2$ .

$$I\ddot{\theta}_f + \tilde{B}\dot{\theta}_f + \tilde{K}\theta_f + F_{du} = k_T \left( \frac{E_{M2} - V_{CEMF}}{R_{armature}} \right) = k_T I_m = AT_m \quad (19)$$

where  $I$  is the equivalent moment of inertia for the fingers, sliding system and the motor armature. We used the damping term  $\tilde{B}$  in order to model all the frictional losses

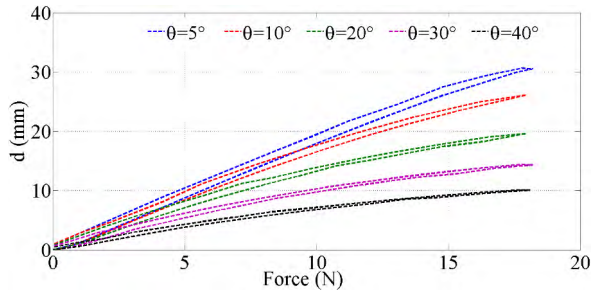


**FIGURE 14.** The hysteresis curves of VSH<sub>1</sub> for different values of the rod angle. To collect these results, we were gradually applying an external force and measuring the associated displacement, *d* and then gradually removing this force.

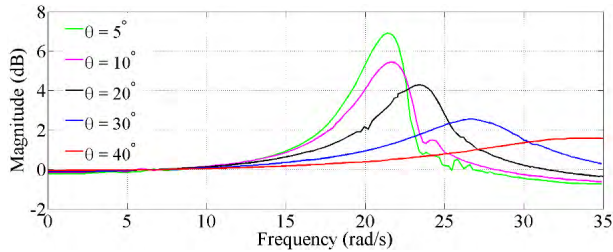


**FIGURE 15.** Magnitude bode plot of VSH<sub>1</sub> for  $\theta = 5^\circ, 10^\circ, 20^\circ, 30^\circ$  and  $40^\circ$ . As expected, the peak magnitude decreases with increasing the stiffness of the fingers.

(the fingers’ joint, *B*, rotor-stator ball bearings, *B<sub>R</sub>*, and the friction between the tendon and pulley and friction of the sliding mechanism, *B<sub>J</sub>*).  $\tilde{K}$  represents the system’s stiffness and *F<sub>du</sub>* is the disturbance-uncertainty term which includes the environmental disturbance force acting upon the fingers as well as any unmodeled parameters of the system. *k<sub>T</sub>*, *E<sub>M2</sub>*, *V<sub>CEMF</sub>* and *R<sub>armature</sub>* are the DC motor’s torque constant, operating voltage, counter-electromotive force (CEMF) and terminal resistance (ohms), respectively. *I<sub>m</sub>* and *T<sub>m</sub>* are the DC motor’s operating current (the current through the motor’s windings) and the motor’s output torque, respectively, and *A* is a constant. For the counter-electromotive of the DC motor we can write:

$$V_{CEMF} = K_e \dot{\theta}_f \tag{20}$$

where *K<sub>e</sub>* is counter-electromotive force constant of the motor. Using (20) we can rewrite (19) as per below:

$$I \ddot{\theta}_f + \tilde{B}' \dot{\theta}_f + \tilde{K} \theta_f + F_{du} = k_{TR} E_{M2} \tag{21}$$

where:

$$\begin{aligned} \tilde{B}' &= \tilde{B} + k_T \frac{K_e}{R_{armature}} \\ k_{TR} &= k_T / R_{armature} \end{aligned} \tag{22}$$

From (21), the state space model of the system can be written as per below:

$$\begin{aligned} X_1 &= \theta_f \\ \dot{X}_1 &= X_2 = \dot{\theta}_f \\ \dot{X}_2 &= \tilde{k}_{TR} E_{M2} - A_{I, \tilde{B}, K, D}(X_1, X_2) \end{aligned} \tag{23}$$

where *X<sub>1</sub>* and *X<sub>2</sub>* are the state variables which, as shown in this equation, are equal to the fingers’ rotational angle and velocity ( $\theta_f, \dot{\theta}_f$ ), respectively. *A<sub>I, B, K, D</sub>* in this equation is a function of state variables and contains the *I*, *B*, *K* and *F<sub>du</sub>* terms, whereas  $\tilde{k}_{TR}$  is the quotient of *I* and *K*.

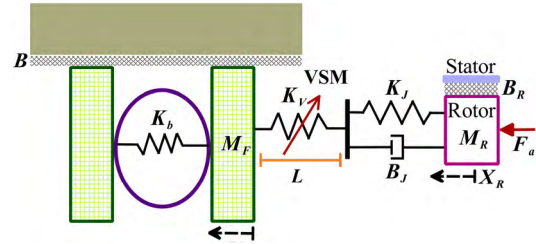


**FIGURE 16.** Schematic model of the two-finger VSH<sub>1</sub> and its M<sub>2</sub>.

It is worth noting that an accurate model of the grasp is hard to determine for several reasons. For instance, let us assume the grasp task in Fig. 16. As shown in this figure, the gripper should grasp an object with the stiffness of *K<sub>b</sub>*. Before the fingers touch the object, the stiffness of the system ( $\tilde{K}$  in (21)) has no effect on the grasp model and hence it is negligible. However, as soon as the fingers start touching the object, the stiffness of the system and the stiffness of the object need to be considered in the grasp model. Unfortunately, there is no way to calculate the stiffness of the unknown objects to be grasped; this makes the grasp model inaccurate. Note that the uncertainty in the object’s stiffness is not the only uncertainty in the grasp. In the design of any control system, and more specifically grasp control, there are always mismatches between the actual system and its dynamical model. These mismatches arise for various reasons such as external disturbances, linearization of nonlinear parameters, neglected and/or unmeasurable parameters (such as friction). In the presence of such uncertainties during grasping tasks and due to unknown external disturbances, utilizing any ordinary control methods will be difficult if not impossible. Robust control methods, and more specifically sliding mode control, however, represent an alternative solution to overcoming such difficulties [53]–[55].

From Fig. 16 it may be noted that, apart from the stabilization effect of the integrated compliant element, this compliant element can be used to control the grip force applied as *F<sub>grip</sub>* = *K<sub>v</sub>* Δ*L*. In order to control this grip force, we designed a sliding mode-based force control method that is explained in the remainder of this section. To design a sliding mode control, we first need to design a sliding variable,  $\sigma(e, \dot{e}, \ddot{e}, \dots)$ . Let us assume an error function as below:

$$e(t) = F_d - F_g \tag{24}$$

where *F<sub>d</sub>* is the desired grip force, whereas *F<sub>g</sub>* is the measured force, the magnitude of which is acquired through a force sensor. The next step in designing a sliding mode control is defining a sliding variable. The sliding variable for the above

error state is given by:

$$\sigma_{(e,\dot{e})}^t = \dot{e} + \eta e, \quad \eta > 0 \quad (25)$$

where  $\eta$  is the convergence rate and any arbitrary positive constant as this guarantees the exponential decay of the error states. In order to achieve asymptotic convergence of the error state variables  $e(t)$  and  $\dot{e}(t)$  to zero,  $\lim t \rightarrow \infty e(t), \dot{e}(t) = 0$ , with a convergence rate  $\eta$ , in the presence of a bounded uncertainty  $|A_{I,\tilde{B},K,D}(X_1, X_2)| \leq \hat{A}$ , the variable  $\sigma$  has to be driven to zero in a finite time. The quasi-sliding mode control law (26) can be used to drive  $\sigma$  to zero in a finite time:

$$\begin{aligned} \omega_R &= -\text{SAT}(\sigma, \varepsilon) \\ \text{SAT}(\sigma, \varepsilon) &= -\Omega\sigma/|\sigma| + \varepsilon \quad \varepsilon \approx 0, \varepsilon > 0 \end{aligned} \quad (26)$$

where the sliding gain,  $\Omega$ , can be calculated as below:

$$\Omega = \hat{A} + \xi/\sqrt{2} \quad (27)$$

The Sliding Mode Control (SMC) input,  $\omega_R$ , in (26) is the rotational velocity of the shaft of  $M_2$ . We use an inner loop anti-windup proportional Integral (PI) controller (shown in Fig. 17) to control this velocity.

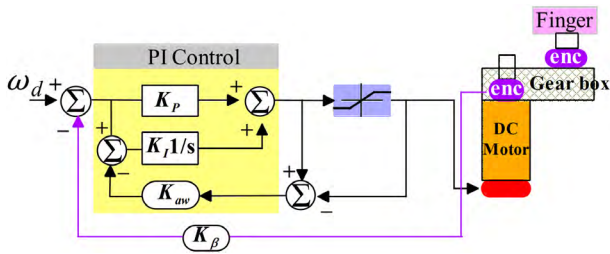


**FIGURE 17.** The anti-windup PI velocity feedback control layout used in  $M_2$ .  $K_p, K_I$  and  $K_{aw}$  represent the proportional, integral and anti-windup gains, respectively;  $K_\beta$  is a conversation gain.

Where  $K_p, K_I$  and  $K_{aw}$  represent the proportional, integral and anti-windup gains, respectively;  $K_\beta$  is a fixed conversation gain.

The role of the term  $\hat{A}$  in (27) is to compensate for the external bounded disturbance and any uncertainty of the system, whilst the term  $\xi/\sqrt{2}$  determines the reaching time to the sliding surface; choosing a larger value for  $\xi$  will lead to a shorter reaching time,  $T_s$ . The sliding manifold reaching time can be calculated as:

$$T_s \leq \frac{2\sqrt{\Lambda_\sigma(0)}}{\xi} = \frac{\sqrt{2}|\sigma(0)|}{\xi} \quad (28)$$

Where  $\Lambda_\sigma$  is the Lyapunov candidate function for the explained SMC design. It is worth noting that from (26), we use the rotational velocity of the shaft of  $M_2$  as the control input in our SMC.

Fig. 18 shows a schematic model of the designed hybrid PI-sliding mode velocity-force controller. Detailed information about the concept and design of the first-order sliding mode controller can be found in [53]–[55].

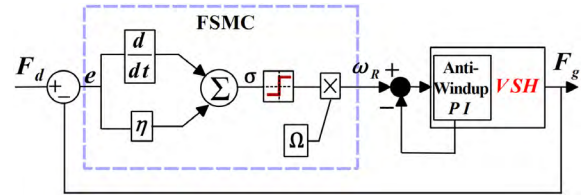


**FIGURE 18.** Schematic model of the hand-PI-SMC. The combination of an inner loop anti-windup speed control and an outer loop first order sliding mode control (FSMC) provides a capability to robustly control the grip force.

## V. STABILITY AND ROBUSTNESS ANALYSIS

In this section we analysis the stability and robustness of the designed controller. To do so, from Fig. 16 and (24) we can write:

$$e(t) = F_d - K_v \Delta L \quad (29)$$

Substituting (29) into (25) we can write:

$$\sigma_{(e,\dot{e})}^t = \dot{F}_d - K_v \dot{\Delta L} + \eta F_d - \eta K_v \Delta L \quad (30)$$

and from (30) we can obtain:

$$\dot{\sigma}_{(e,\dot{e})}^t = \ddot{F}_d - K_v \ddot{\Delta L} + \eta \dot{F}_d - \eta K_v \dot{\Delta L} \quad (31)$$

where for  $\eta K_v \dot{\Delta L}$  we can write:

$$\eta K_v \dot{\Delta L} = \eta K_v \dot{\Delta L} + \dot{\Delta L} - \dot{\Delta L} = \underbrace{(\eta K_v - 1)}_H \dot{\Delta L} + \dot{\Delta L} \quad (32)$$

Substituting (32) into (31) we can get:

$$\begin{aligned} \dot{\sigma}_{(e,\dot{e})}^t &= \underbrace{\ddot{F}_d - K_v \ddot{\Delta L} + \eta \dot{F}_d - H \dot{\Delta L}}_{A(\dot{\Delta L}, K_v, t)} - \dot{\Delta L} \\ &\Rightarrow \dot{\sigma} = A(\dot{\Delta L}, K_v, t) - \dot{\Delta L} \end{aligned} \quad (33)$$

where  $\dot{\Delta L}$  and  $\ddot{\Delta L}$  are the speed and acceleration of the slider in the sliding system which are measurable using the encoder. The variable  $A(\dot{\Delta L}, K_v, t)$  in (33) is called the system's cumulative uncertainty-disturbance. We assume that this term is bounded,  $|A(\dot{\Delta L}, K_v, t)| \leq \hat{A}$ .

As explained above and from (24) and (25), driving the sliding variable to zero in finite time leads to an asymptotic convergence to zero on the error state variables  $e(t)$  and  $\dot{e}(t)$ . In order to drive the sliding variable to zero, the controller should satisfy the following reachability condition [55]:

$$\sigma \dot{\sigma} \leq -\bar{\xi} |\sigma|, \quad \text{where } \bar{\xi} = \frac{\xi}{\sqrt{2}} \quad (34)$$

where from (33) we can write:

$$\sigma \dot{\sigma} = \sigma (A(\dot{\Delta L}, K_v, t) - \dot{\Delta L}) \leq |\sigma| \hat{A} - \sigma \dot{\Delta L} \quad (35)$$

and selecting:

$$\dot{\Delta L} = \tilde{\Omega} \text{sign}(\sigma) \quad (36)$$

by substituting (36) into (35) and from (34) we obtain:

$$\sigma \dot{\sigma} \leq |\sigma| (\hat{A} - \tilde{\Omega}) = -\bar{\xi} |\sigma| \quad (37)$$

From (37) we can conclude that the sliding mode gain should satisfy the reachability condition shown by (38) in order to guarantee the stability and robustness of the designed controller for a bounded disturbance-uncertainty,  $A(\Delta L, K_v, t)$ .

$$\tilde{\Omega} \geq \dot{A} + \tilde{\xi} \tag{38}$$

The term  $\dot{A}$  in (38) is used to overcome  $A(\Delta L, K_v, t)$ , whilst the second term,  $\tilde{\xi}$ , determines the reaching time to the sliding surface; this reaching time can be calculated by substituting  $\tilde{\xi}$  into (28). Any controller gain that satisfy condition (38) guarantees the stability of the designed controller.

**VI. CONTROL TEST PLATFORM**

Fig. 19 shows the two-finger version of VSH<sub>1</sub> as mounted on an ABB IRB 1200 with a 7 kg payload. We used this platform to test the controller. The grip force feedback is provided by a force sensor that was obtained from a 1D Force Sensing Resistor (FSR) mounted on the right fingertip. The cost of the sensor was £9. The main technical specifications of the sensor are reported in Table 2.

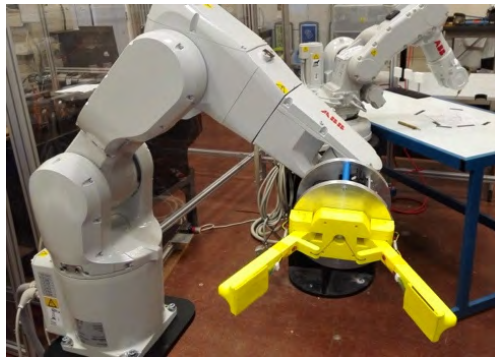


**FIGURE 19.** The two-finger VSH<sub>1</sub> mounted on the ABB robot.

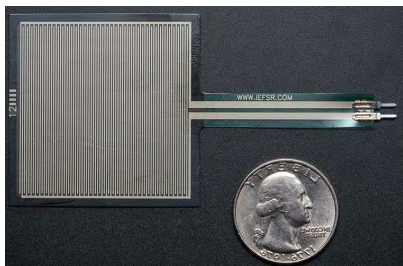


**FIGURE 20.** Force Sensing Resistor used for the tests.

The sensor (shown in Fig. 20) provides an analogue output as a variable resistance. We use a voltage divider circuit to transform the value of the resistance to a voltage value, which is readable by our control system. To emulate objects of different mechanical stiffnesses,  $K_b$ , we designed a variable stiffness object (VSO), wherein springs with different stiffness can be exchanged.

As shown in Fig. 21 the VSO consists of a spring in the center which can be replaced to alter the stiffness of the object.

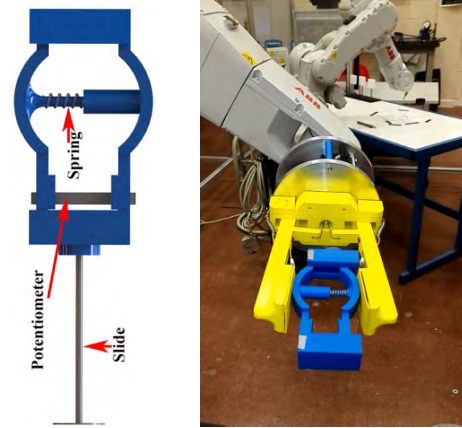


**FIGURE 21.** The VSO, Variable Stiffness Object, used in this paper.

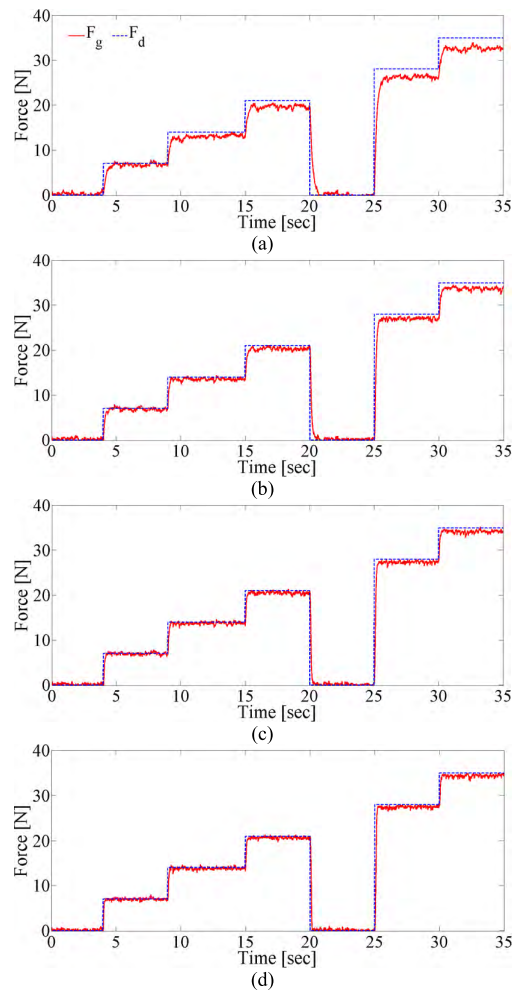


**FIGURE 22.** Force tracking test with VSH<sub>1</sub> for (a)  $\theta = 0^\circ$  and  $K_b = 1$  (b)  $\theta = 5^\circ$  and  $K_b = 1.25$  (c)  $\theta = 10^\circ$  and  $K_b = 2.6$  (d)  $\theta = 15^\circ$  and  $K_b = 3.3$  N/mm. The dashed blue lines and solid red lines are the desired trajectory and the response of the designed controller to the desired trajectory input, respectively. (e) The sliding variable,  $\sigma$ , for this experiment.

The VSO also consists of a linear potentiometer to measure the deformation of the VSO for our records. This data is then measured using an Arduino Mega, and sent via serial communication to a Windows PC using a baud rate of 9600 bps.

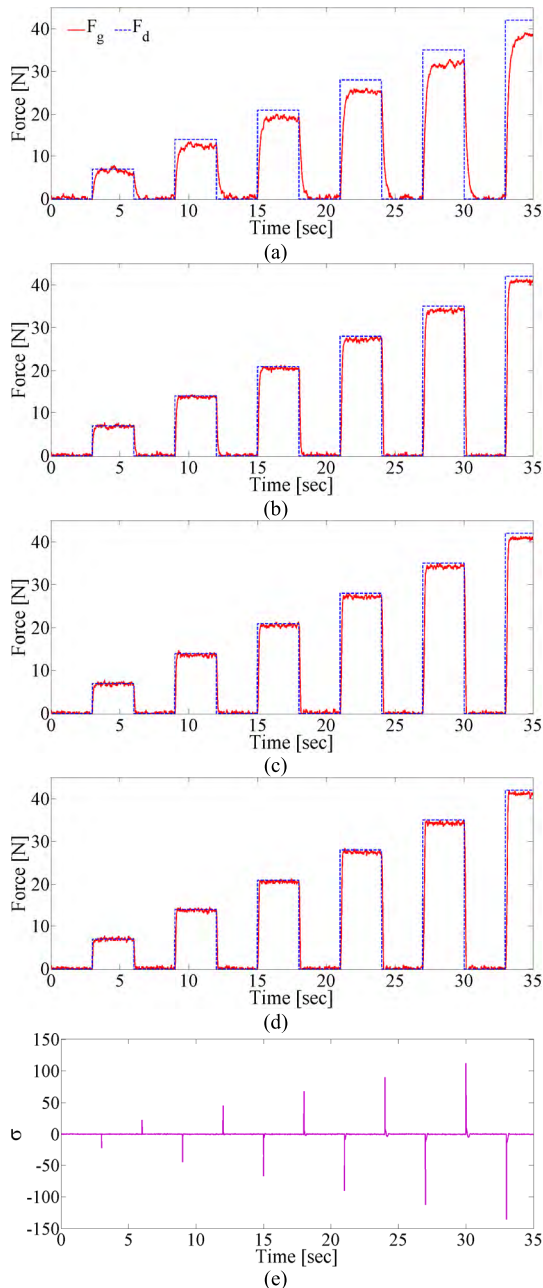


**FIGURE 23.** Response of the hand controlled by the designed controller (solid red lines) to the step inputs with increasing amplitude (dashed blue lines) for (a)  $\theta = 0^\circ$  and  $K_b = 1$  (b)  $\theta = 5^\circ$  and  $K_b = 1.25$  (c)  $\theta = 10^\circ$  and  $K_b = 2.6$  (d)  $\theta = 15^\circ$  and  $K_b = 3.3$  N/mm (e) The sliding variable,  $\sigma$ , for this experiment.

We used four compression springs with different stiffness constants in our tests.

Fig. 22 and 23 (a), (b), (c) and (d) depict the experimental results for the force control architecture explained by (26) and (27) and for the VSO with stiffnesses of  $K_b = 1, 1.25, 2.6$  and  $3.3$  N/mm, respectively. To collect this data, the angle  $\theta$  was set to  $0, 5, 10$  and  $15$  degrees, respectively. The control gain and the error convergence rate in these tests were  $\Omega = 220$  degree/sec and  $\eta = 20$ . The dashed blue lines

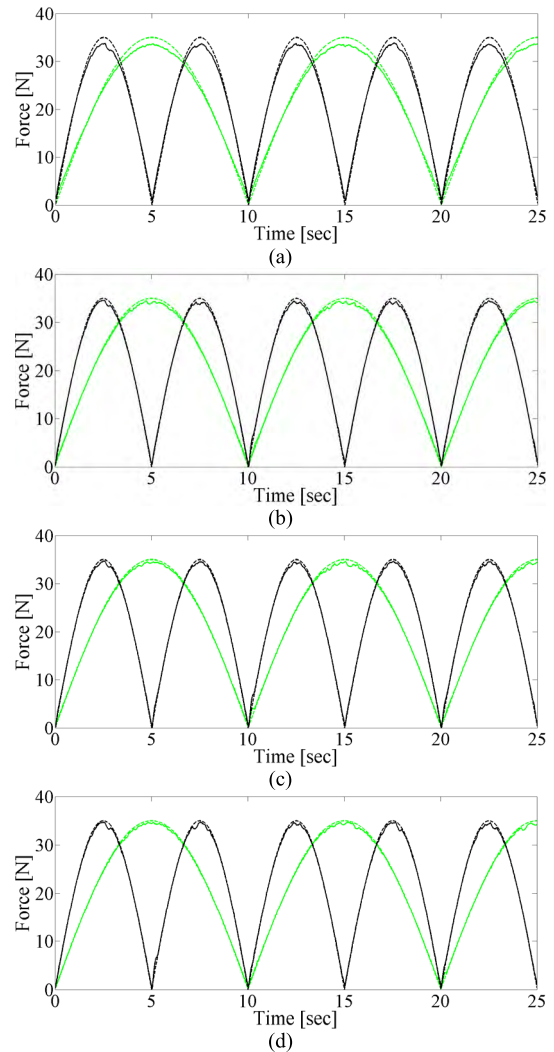


**FIGURE 24.** Response of the hand controlled by the designed controller (solid lines) to the sinusoidal inputs (dashed lines) for (a)  $\theta = 0^\circ$  and  $K_b = 1$  (b)  $\theta = 5^\circ$  and  $K_b = 1.25$  (c)  $\theta = 10^\circ$  and  $K_b = 2.6$  (d)  $\theta = 15^\circ$  and  $K_b = 3.3$  N/mm.

in subplots a, b, c and d in these figures depict the desired grip force,  $F_d$ , whereas the red curves show the measured force,  $F_g$ . As the figures show, thanks to the robustness of the designed SMC to overcoming uncertainty and environmental disturbances, the output of the controller always follows the desired input values with negligible overshoot and small steady-state errors. By comparing these subplots, it may also be noted that the steady-state errors decrease with increasing angle  $\theta$ . This can be explained by the fact that the hysteresis band in  $VSH_1$  also decreases with increasing  $\theta$  (please recall Fig. 14). Finally, the error-based sliding variable  $\sigma(e, \dot{e})$  for these tests is shown in subplot (e) of the figures. As these subplots show, the sliding variable always remains at zero except at the moment when the desired grip force changes. This demonstrates the robustness of the designed controller in driving the error states to zero. At the instant that  $F_d$  changes, the sliding variable jumps above or below zero for a very short period, then the controller drove it to zero. This proves the

robustness of the controller in converging the error states to zero in a finite time.

Fig. 23 (a), (b), (c) and (d) depict the experimental results of the controller for two sinusoidal inputs and for the variable sets as  $\langle K_b = 1\text{N/mm}, \theta = 0^\circ \rangle$ ,  $\langle K_b = 1.25\text{N/mm}, \theta = 5^\circ \rangle$ ,  $\langle K_b = 2.6\text{N/mm}, \theta = 10^\circ \rangle$  and  $\langle K_b = 3.3\text{N/mm}, \theta = 15^\circ \rangle$ , respectively. In this figure, the dashed black and green curves depict the desired grip force, whereas the solid black and green curves show the measured grip force,  $F_g$ . As the figures show, the output of the controller always follows the desired sinusoidal inputs, with zero overshoot and small steady-state errors. Similar to the previous experiments, in this experiment the steady-state errors decrease with increasing angle  $\theta$ .

## VII. CONCLUSION

A novel variable stiffness mechanism has been presented in this paper. The mechanism introduced provides a driving force for tendon-driven hands with an ability to control the position and stiffness of the fingers. The design consisted of two rotational servomotors. One of the servomotors, along with an integrated linear compression spring, was used to control the stiffness of the fingers whereas the other motor was responsible for changing the fingers' positions. In order to control the apparent stiffness in the fingers, a mathematical model of the stiffness as a function of the shaft angle has been derived. Experimental results confirmed the effectiveness of the proposed variable stiffness mechanism. The hand design introduced is characterized by a large variability in stiffness, which is an essential requirement for a highly flexible handling system, and is particularly useful in food industry scenarios. The hand is also characterized by its fast response and small hysteresis band. The simplicity of its design besides providing a low-cost solution, guarantees the inherent reliability and robustness of this mechanism. The mechanism introduced can be used to control the grip force applied through simple control of the stiffness and compression of the integrated spring. Moreover, as explained, the integrated serial compliant element increases the robustness of the fixed gain controllers when dealing with objects of uncertain stiffness. In this paper we explained a PI-first order sliding mode velocity-force control architecture we designed to control the grip force by controlling the compression of the spring in the variable stiffness mechanism. We have shown experimentally, in the presence of unknown external disturbances and uncertainty of the model, that the designed SMC can robustly and in a finite time converge the error state variables to the origin and hence obtain the desired spring compression and, as a result, the desired grip force.

## REFERENCES

- [1] C.-H. Wu, J.-C. Houk, K.-Y. Young, and L. E. Miller, "Nonlinear damping of limb motion," in *Multiple Muscle Systems*. New York, NY, USA: Springer, 1990, pp. 214–235.
- [2] A. Esteki and J. M. Mansour, "An experimentally based nonlinear viscoelastic model of joint passive moment," *J. Biomech.*, vol. 29, no. 4, pp. 443–450, 1996.
- [3] N. Shrivastava, M. F. Koff, A. E. Abbot, V. C. Mow, M. P. Rosenwasser, and R. J. Strauch, "Simulated extension osteotomy of the thumb metacarpal reduces carpometacarpal joint laxity in lateral pinch," *J. Hand Surgery*, vol. 28, no. 5, pp. 733–738, 2003.
- [4] A. Minami, K.-N. An, W. P. Cooney, III, R. L. Linscheid, and E. Y. S. Chao, "Ligament stability of the metacarpophalangeal joint: A biomechanical study," *J. Hand Surgery*, vol. 10, no. 2, pp. 255–260, 1985.
- [5] K. Tamai, J. Ryu, K. N. An, R. L. Linscheid, W. P. Cooney, and E. Y. S. Chao, "Three-dimensional geometric analysis of the metacarpophalangeal joint," *J. Hand Surgery*, vol. 13, no. 2, pp. 521–529, 1988.
- [6] P.-H. Kuo and A. D. Deshpande, "Muscle-tendon units provide limited contributions to the passive stiffness of the index finger metacarpophalangeal joint," *J. Biomech.*, vol. 45, no. 15, pp. 2531–2538, 2012.
- [7] J. Qin, D. Lee, Z. Li, H. Chen, and J. T. Dennerlein, "Estimating *in vivo* passive forces of the index finger muscles: Exploring model parameters," *J. Biomech.*, vol. 43, no. 7, pp. 1358–1363, 2010.
- [8] M. C. Carrozza et al., "A cosmetic prosthetic hand with tendon driven under-actuated mechanism and compliant joints: Ongoing research and preliminary results," in *Proc. IEEE Int. Conf. Robot. Autom. (ICRA)*, Apr. 2005, pp. 2661–2666.
- [9] M. C. Carrozza et al., "On the development of a novel adaptive prosthetic hand with compliant joints: Experimental platform and EMG control," in *Proc. IEEE/RSJ Int. Conf. Intell. Robots Syst. (IROS)*, Aug. 2005, pp. 1271–1276.
- [10] B. Tondu, V. Boitier, and P. Lopez, "Naturally compliant robot-arms actuated by McKibben artificial muscles," in *Proc. IEEE Int. Conf. Syst., Man, Cybern.*, vol. 3, Oct. 1994, pp. 2635–2640.
- [11] M. C. Carrozza, B. Massa, S. Micera, M. Zecca, and P. Dario, "A wearable artificial hand for prosthetics and humanoid robotics applications," in *Proc. IEEE-RAS Int. Conf. Humanoid Robots*, Nov. 2001.
- [12] C. E. English and D. Russell, "Mechanics and stiffness limitations of a variable stiffness actuator for use in prosthetic limbs," *Mechanism Mach. Theory*, vol. 34, no. 1, pp. 7–25, 1999.
- [13] R. J. Christensen, "Prosthetic foot with energy transfer medium including variable viscosity fluid," U.S. Patent 6663 673 B2, Dec. 16, 2003.
- [14] G. A. Pratt and M. M. Williamson, "Series elastic actuators," in *Proc. IEEE/RSJ Int. Conf. Intell. Robots Syst., Hum. Robot Interact. Cooperat. Robots*, vol. 1, Aug. 1995, pp. 399–406.
- [15] D. W. Robinson, J. E. Pratt, D. J. Paluska, and G. A. Pratt, "Series elastic actuator development for a biomimetic walking robot," in *Proc. IEEE/ASME Int. Conf. Adv. Intell. Mechatronics*, Sep. 1999, pp. 561–568.
- [16] G. A. Pratt and M. M. Williamson, "Series elastic actuators," presented at the IROS, Pittsburgh, PA, USA, Aug. 1995.
- [17] D. W. Robinson and G. A. Pratt, "Force controllable hydro-elastic actuator," in *Proc. IEEE Int. Conf. Robot. Autom. (ICRA)*, vol. 2, Apr. 2000, pp. 1321–1327.
- [18] N. G. Tsagarakis, M. Laffranchi, B. Vanderborght, and D. G. Caldwell, "A compact soft actuator unit for small scale human friendly robots," in *Proc. IEEE Int. Conf. Robot. Autom. (ICRA)*, May 2009, pp. 4356–4362.
- [19] N. G. Tsagarakis, I. Sardellitti, and D. G. Caldwell, "A new variable stiffness actuator (CompAct-VSA): Design and modelling," in *Proc. IEEE/RSJ Int. Conf. Intell. Robots Syst. (IROS)*, Sep. 2011, pp. 378–383.
- [20] K. Kong, J. Bae, and M. Tomizuka, "A compact rotary series elastic actuator for human assistive systems," *IEEE/ASME Trans. Mechatronics*, vol. 17, no. 2, pp. 288–297, Apr. 2012.
- [21] H. Woo, B. Na, and K. Kong, "Design of a compact rotary series elastic actuator for improved actuation transparency and mechanical safety," in *Proc. IEEE Int. Conf. Robot. Autom. (ICRA)*, May/June 2017, pp. 1872–1877.
- [22] G. Tonietti, R. Schiavi, and A. Bicchi, "Design and control of a variable stiffness actuator for safe and fast physical human/robot interaction," in *Proc. IEEE Int. Conf. Robot. Autom. (ICRA)*, Apr. 2005, pp. 526–531.
- [23] A. Bicchi, G. Tonietti, M. Bavaro, and M. Piccigallo, "Variable stiffness actuators for fast and safe motion control," in *Proc. 11th Int. Symp. Robot. Res.* Berlin, Germany: Springer, 2005, pp. 527–536.
- [24] T. Inoue, R. Miyata, and S. Hirai, "Force control on antagonistic twist-drive actuator robot," in *Proc. IEEE/RSJ Int. Conf. Intell. Robots Syst. (IROS)*, Oct. 2016, pp. 3830–3835.
- [25] R. Van Ham, B. Vanderborght, M. Van Damme, B. Verrelst, and D. Lefeber, "MACCEPA: The mechanically adjustable compliance and controllable equilibrium position actuator for controlled passive walking," in *Proc. IEEE Int. Conf. Robot. Autom. (ICRA)*, May 2006, pp. 2195–2200.

- [26] R. Van Ham, B. Vanderborght, M. Van Damme, B. Verrelst, and D. Lefeber, "MACCEPA, the mechanically adjustable compliance and controllable equilibrium position actuator: Design and implementation in a biped robot," *Robot. Auto. Syst.*, vol. 55, no. 2, pp. 761–768, 2007.
- [27] B. Vanderborght, N. G. Tsagarakis, C. Semini, R. Van Ham, and D. G. Caldwell, "MACCEPA 2.0: Adjustable compliant actuator with stiffening characteristic for energy efficient hopping," in *Proc. IEEE Int. Conf. Robot. Automat. (ICRA)*, May 2009, pp. 544–549.
- [28] S. Wolf and G. Hirzinger, "A new variable stiffness design: Matching requirements of the next robot generation," in *Proc. IEEE Int. Conf. Robot. Automat. (ICRA)*, May 2008, pp. 1741–1746.
- [29] V. Chalvet and D. J. Braun, "Algorithmic design of low-power variable-stiffness mechanisms," *IEEE Trans. Robot.*, vol. 33, no. 6, pp. 1508–1515, Dec. 2017.
- [30] M. Grebenstein and P. van der Smagt, "Antagonism for a highly anthropomorphic hand–arm system," *Adv. Robot.*, vol. 22, no. 1, pp. 39–55, 2008.
- [31] M. Grebenstein et al., "The hand of the DLR hand arm system: Designed for interaction," *Int. J. Robot. Res.*, vol. 31, no. 13, pp. 1531–1555, 2012.
- [32] M. Grebenstein, M. Chalon, G. Hirzinger, and R. Siegart, "Antagonistically driven finger design for the anthropomorphic DLR hand Arm system," in *Proc. 10th IEEE-RAS Int. Conf. Humanoid Robots*, Dec. 2010, pp. 609–616.
- [33] R. S. Johansson and G. Westling, "Programmed and triggered actions to rapid load changes during precision grip," *Exp. Brain Res.*, vol. 71, no. 1, pp. 72–86, 1988.
- [34] K. Tahara, Z.-W. Luo, R. Ozawa, J.-H. Bae, and S. Arimoto, "Bio-mimetic study on pinching motions of a dual-finger model with synergistic actuation of antagonist muscles," in *Proc. Int. Conf. Robot. Automat. (ICRA)*, May 2006, pp. 994–999.
- [35] A. D. Deshpande, N. Gialias, and Y. Matsuoka, "Contributions of intrinsic visco-elastic torques during planar index finger and wrist movements," *IEEE Trans. Biomed. Eng.*, vol. 59, no. 2, pp. 586–594, Feb. 2012.
- [36] P.-H. Kuo, J. DeBacker, and A. D. Deshpande, "Design of robotic fingers with human-like passive parallel compliance," in *Proc. IEEE Int. Conf. Robot. Automat. (ICRA)*, May 2015, pp. 2562–2567.
- [37] T. D. Niehues, P. Rao, and A. D. Deshpande, "Compliance in parallel to actuators for improving stability of robotic hands during grasping and manipulation," *Int. J. Robot. Res.*, vol. 34, no. 3, pp. 256–269, 2015.
- [38] S. Kajikawa and K. Abe, "Development of robot hand with multi-directional variable stiffness for human-care services," in *Proc. IEEE/RSJ Int. Conf. Intell. Robots Syst. (IROS)*, Oct. 2012, pp. 2889–2894.
- [39] Y. Yang and Y. Chen, "Novel design and 3D printing of variable stiffness robotic fingers based on shape memory polymer," in *Proc. 6th IEEE Int. Conf. Biomed. Robot. Biomechanics (BioRob)*, Jun. 2016, pp. 195–200.
- [40] H. K. Yap, J. H. Lim, F. Nasrallah, J. C. H. Goh, and R. C. H. Yeow, "A soft exoskeleton for hand assistive and rehabilitation application using pneumatic actuators with variable stiffness," in *Proc. IEEE Int. Conf. Robot. Automat. (ICRA)*, May 2015, pp. 4967–4972.
- [41] L. U. Odhner et al., "A compliant, underactuated hand for robust manipulation," *Int. J. Robot. Res.*, vol. 33, no. 2, pp. 736–752, 2014.
- [42] P.-H. Kuo and A. D. Deshpande, "Novel design of a passive variable stiffness joint mechanism: Inspiration from biomechanics of hand joints," in *Proc. ASME Dyn. Syst. Control Conf.*, Oct. 2013, p. V002T28A003.
- [43] A. M. Dollar and R. D. Howe, "The highly adaptive SDM hand: Design and performance evaluation," *Int. J. Robot. Res.*, vol. 29, no. 5, pp. 585–597, 2010.
- [44] A. M. Dollar and R. D. Howe, "A robust compliant grasper via shape deposition manufacturing," *IEEE/ASME Trans. Mechatronics*, vol. 11, no. 2, pp. 154–161, Apr. 2006.
- [45] A. M. Dollar and R. D. Howe, "Towards grasping in unstructured environments: Grasper compliance and configuration optimization," *Adv. Robot.*, vol. 19, no. 5, pp. 523–543, 2005.
- [46] A. Pettersson, S. Davis, J. O. Gray, T. J. Dodd, and T. Ohlsson, "Design of a magnetorheological robot gripper for handling of delicate food products with varying shapes," *J. Food Eng.*, vol. 98, no. 3, pp. 332–338, 2010.
- [47] H. Maekawa, K. Yokoi, K. Tanie, M. Kaneko, N. Kimura, and N. Imamura, "Development of a three-fingered robot hand with stiffness control capability," *Mechatronics*, vol. 2, no. 5, pp. 483–494, 1992.
- [48] C. Y. Lau and A. Chai, "The development of a low cost pneumatic air muscle actuated anthropomorphic robotic hand," *Procedia Eng.*, vol. 41, pp. 737–742, Jul. 2012.
- [49] S. Rasakatla and K. M. Krishna, "RAMA-1 highly dexterous 48DOF robotic hand using magnetic spherical joints," in *Proc. IEEE Int. Conf. Robot. Biomimetics (ROBIO)*, Dec. 2013, pp. 816–823.
- [50] C. Ott, A. Albu-Schäffer, A. Kugi, and G. Hirzinger, "On the passivity-based impedance control of flexible joint robots," *IEEE Trans. Robot.*, vol. 24, no. 2, pp. 416–429, Apr. 2008.
- [51] M. G. Catalano et al., "VSA-Cubebot: A modular variable stiffness platform for multiple degrees of freedom robots," in *Proc. IEEE Int. Conf. Robot. Automat. (ICRA)*, May 2011, pp. 5090–5095.
- [52] S. V. Drakunov and V. I. Utkin, "Sliding mode control in dynamic systems," *Int. J. Control*, vol. 55, no. 4, pp. 1029–1037, 1992.
- [53] V. Utkin, J. Guldner, and J. Shi, *Sliding Mode Control in Electro-Mechanical Systems*. Boca Raton, FL, USA: CRC Press, 2017.
- [54] Y. Shtessel, C. Edwards, L. Fridman, and A. Levant, *Sliding Mode Control and Observation*, vol. 978. New York, NY, USA: Birkhäuser Verlag, 2014, p. 10.



**SABER MAHBOUBI** received the bachelor's degree in power engineering from the University of Rajae, Tehran, Iran, in 2006, and the M.Sc. degree in mechatronics from the University of Tabriz, Iran, in 2010. He then became a Researcher Fellow with the Max Planck Institute for Biological Cybernetics, Germany. He is currently pursuing the Ph.D. degree (Marie Curie) with the University of Salford, Manchester, U.K. His research interests include biologically inspired systems, variable impedance mechanisms, robust control, and artificial intelligence.



**STEVEN DAVIS** received the degree in robotic and electronic engineering from the University of Salford in 1998, the M.Sc. degree in advanced robotics in 2000, and the Ph.D. degree in 2005. He became a Research Fellow before moving to the Italian Institute of Technology in 2008 as a Team Leader. In 2012, he returned to the University of Salford as a Lecturer in manufacturing automation and robotics. He has published extensively and has also co-authored chapters in two books on automation. He has experience of attracting research funding, most notably the €3,948,470 Marie Curie Initial Training Networks Sustainable Manufacturing through Advanced Robotics Training in Europe. His research interests include actuators, biologically inspired systems, biomimetics, soft robotics, humanoid robots, end-effectors and dexterous hands, and industrial automation, particularly in the food industry. He has been associate editor of several IEEE conferences and is a Guest Editor of a special edition of the journal *Actuators*.



**SAMIA NEFTI-MEZIANI** received the Ingeniorat d'etat and DEA degrees in industrial engineering and the Doctorat D'etat (Ph.D.) degree in robotics. She currently holds the Chair in robotics and is the Director of the Centre for Autonomous Systems and Advanced Robotics, University of Salford. She has a well-established track record and has published extensively in the areas of advanced robotics and autonomous systems. She is the Coordinator of the European Marie Curie Innovative Training Network SMART-E and the coordinator and CO-I of three further Major national programmes worth more than £14M. She is the Vice Chairman of the IEEE Robotics and Automation U.K. and RI, an Associate Editor of the IEEE Transactions on Fuzzy Systems and a Member of the Advisory Board of the U.K. Research Council EPSRC. She serves on the Advisory Board of the EPSRC National Centre in Innovative Manufacturing. She is one the Founder members of the Northern Robotics and Autonomous Systems Network which is part of the Innovate U.K. Network.

...